The small-scale kinematics of a variable-density turbulent jet

Chris Lai[1*], John Charonko[1], Kathy Prestridge[1]

[1] Los Alamos National Laboratory, P-23 Physics Division, Los Alamos, New Mexico, USA

* chrislck@lanl.gov

Abstract

We present the experimental results of a turbulent variable-density (VD) jet inside a wind tunnel. Our goal is to study the differences in the kinematics and dynamics of the small scales between constant- and VD flows – the knowledge is important to the development of physics-based turbulence closure models. To obtain the full velocity gradient tensor (VGT) needed in the analysis, we used time-resolved stereoscopic particle image velocimetry (SPIV) together with the Taylor's *frozen turbulence* hypothesis to reconstruct the jet volume at a streamwise location that was sixteen jet diameters ($16D$) from the jet nozzle. We found the following for the dense SF_6 jet: (1) it experiences less fluid deformation (left panel in figure 3), (2) it has a weaker normalized vortex-stretching term, and (3) conditional statistics based on the different quadrants in the QR-plot show that it has stronger enstrophy production/destruction contributions to the total $\omega_i s_{ij} \omega_j$ than that observed in the air jet.

1 Introduction

Turbulent flows involving variable densities are commonly found in the atmosphere, ocean, and industrial processes. In flows where the variations in fluid density are small, fluid inertia is essentially unaltered and the varying density can be treated as a source of buoyancy only. This is the Boussinesq approximation for small density differences, and it implies symmetry in mixing behaviors *i.e.* heavy-into-light and light-into-heavy fluids behave the same. When the density variations are large, the non-negligible differential momentum of fluid parcels create asymmetry in mixing behaviors (Livescu and Ristorcelli, 2007, 2008). This brings interesting observations such as the recently observed negative turbulent kinetic energy (t.k.e.) production at the centerline of a dense sulphur hexaflouride (SF_6) jet discharged into a coflowing stream of air (Charonko and Prestridge, 2017). A negative t.k.e. production is indicative of a small-to-large scale energy transfer. In a follow-up paper, Lai et al. (2018) identifies the stretching of turbulent eddies by mean flow gradients as the physical mechanism responsible for the negative production.

To better understand the effects of variable density on the phenomenology of the small scales, we present an experimental study on variable-density turbulent jets, which is a continuation of our earlier works (Charonko and Prestridge, 2017; Lai et al., 2018). In §2, we briefly review the tool used to study behaviors of small scales in turbulence - the scalar invariants of the velocity gradient tensor (VGT). In §3, we gives the details of our experiments and describe how we obtain the full VGT from the data. We then examine the fluid deformation and the mechanism of vortex-stretching in §4, followed by a conclusion in §5.

2 Theory

Fluid turbulence is a multiscale phenomenon which strongly couples a wide range of spatio-temporal scales together by nonlinearities (Pope, 2000). It is a physical process characterized by the continuous generation of velocity derivatives - both in space and time (Tsinober, 2009). Because the derivative is mostly contributed by the small scales, the velocity gradient tensor (VGT) $\mathbf{A} = A_{ij} = \partial u_i / \partial x_j$, where $\mathbf{u}$ is the zero-mean fluctuating velocity, contains a wealth of information on the behaviors of small scales (Meneveau, 2011). This is seen in the transport equations of the enstrophy $\omega_i \omega_i$ ($\omega = \nabla \times \mathbf{u} = \varepsilon_{ijk} A_{kj}$), and the square of the

Frobenius norm $\sqrt{s_{ij}s_{ij}}$ of the rate-of-strain tensor $\mathbf{s} = (\mathbf{A} + \mathbf{A}^{\mathrm{T}})/2$. For incompressible flows, the equations are:

$$\frac{1}{2}\frac{D(s_{ij}s_{ij})}{Dt} = \overbrace{-s_{ij}s_{jk}s_{ki}}^{\text{strain self-amplification}} - \frac{1}{4}\omega_i s_{ij}\omega_j - s_{ij}\frac{\partial^2 p}{\partial x_i \partial x_j} + \nu s_{ij}\triangle s_{ij} \tag{1}$$

$$\frac{1}{2}\frac{D\omega^2}{Dt} = \overbrace{\omega_i s_{ij}\omega_j}^{\text{vortex-stretching}} + \nu \omega_i \triangle \omega_i \tag{2}$$

In both equations, the terms under the curly bracket on the r.h.s can be positive or negative. They are, however, positive on average and thus represent source terms in turbulent flows (Tsinober, 2009). In particular, the strain amplification term in eq.(1) is responsible for creating intense dissipative regions in turbulent flows whereas the vortex-stretching term in eq.(2) is interpreted to be the physical mechanism responsible for interscale energy transfer in turbulence. The spatio-temporal correlation of dissipation and enstrophy in turbulent flows is an active research area to understand the phenomenology of turbulence (Ooi et al., 1999).

The velocity gradient tensor is a second-rank tensor and has three scalar principal invariants (invariant under any orthogonal rotations of the coordinate system): $P = \mathrm{Tr}(\mathbf{A}) = \frac{\partial u_i}{\partial x_i}$, $Q = -\frac{1}{2}\mathrm{Tr}(\mathbf{A}\mathbf{A}^{\mathrm{T}})$ and $R = -\mathrm{Det}(\mathbf{A})$, collectively known as the *first*, *second* and *third* principal invariants. For our air and SF_6 jets, the flow is essentially incompressible, leading to $P = 0$. The joint probability density function (PDF) between Q and R - the QR-plot - is a tool used to infer local flow topologies and to study the mechanism of vortex-stretching in turbulent flows (Chong et al., 1990).

In eq.(1) and (2), s_{ij} and ω_i is related to the symmetric and skew-symmetric parts of $\mathbf{A} = \mathbf{s} + \Omega$, respectively. The skew-symmetric spin tensor $\Omega = (\mathbf{A} - \mathbf{A}^{\mathrm{T}})/2$ is related to ω_i by $\omega_i = -\varepsilon_{ijk}\Omega_{jk}$. Both $\mathbf{s}$ and Ω have their own principal invariants - (1) $P_s = P = \mathrm{Tr}(\mathbf{s})$, $Q_s = -\frac{1}{2}s_{ij}s_{ij}$, $R_s = -\frac{1}{3}s_{ij}s_{jk}s_{ki}$ and (2) $P_\Omega = 0$, $Q_\Omega = \frac{1}{2}\Omega_{ij}\Omega_{ij} = \frac{1}{4}\omega_i\omega_i$, $R_\Omega = -\frac{1}{4}\omega_i s_{ij}\omega_j$. The strain self-amplification and vortex-stretching terms can be expressed as the following,

$$-3R_s = s_{ij}s_{jk}s_{ki} = \alpha^3 + \beta^3 + \gamma^3 \tag{3}$$

$$-4R_\Omega = \omega_i s_{ij}\omega_j = \omega_k^2 \alpha \cos^2(\omega, e_\alpha) + \omega_k^2 \beta \cos^2(\omega, e_\beta) + \omega_k^2 \gamma \cos^2(\omega, e_\gamma) \tag{4}$$

where (α, β, γ) and $(e_\alpha, e_\beta, e_\gamma)$ are the set of eigenvalues/vectors of $\mathbf{s}$. The third invariants of $\mathbf{s}$ and Ω thus represent the generation/destruction of strains and enstrophy in turbulent flows. Together with their second invariants (Q_s, Q_Ω) that characterize whether a flow region is dominated by strains or enstrophy (swirling motions), they form a complete set of tools to study the behaviors of fine-scale turbulence. We apply the above formulation to a turbulent variable-density jet.

3 Experiments

To obtain all nine components of the VGT, simultaneous measurements of the turbulent velocity field inside a three-dimensional fluid volume is needed. This can be realized using holographic or volumetric particle image velocimetry (PIV) (Westerweel et al., 2013). The experimental setup usually consists of multiple independent camera views with the understanding that the accuracy of flow measurements increases with the number of cameras, or with the use of just one camera together with a more elaborate optical setup and post processing routines as realized in the experiments reported by Zhang et al. (1997). For turbulent flows having a dominant convecting velocity in one direction, it is possible to bypass the requirement of a true volumetric measurement - by using Taylor's *frozen turbulence* hypothesis to turn temporal information into spatial information along the direction of the convecting velocity. Its root can be traced back to hot-wire measurements in which the turbulent velocity at a spatial location, a few micros large, is rapidly sampled in time in excess of kilohertz. The temporal frequency is usually much higher than the shortest temporal scale in the flow and therefore the fluctuating velocity field appears to be frozen and it can be treated as being passively convected downstream without any distortions. Applying the hypothesis to convectional

two-dimensional PIV is an alternative to volumetric PIV because it provides full field measurement over a region. A number of previous studies have employed this technique to study behaviors of small-scale turbulence in a constant-density air jet (Ganapathisubramani et al., 2008) and in space-filling, fractal square grids (Gomes-Fernandes et al., 2014). We employ this technique to acquire the data needed to analyze the behaviors of small-scale turbulence in a variable-density jet.

The experimental facility is a 5m-tall, open-circuit wind tunnel located at the Los Alamos National Laboratory. Details of this facility are described in Charonko and Prestridge (2017), and we give a brief description of our setup in the following. Figure 1 shows a schematic of the present setup. The wind tunnel has a square cross-section of 0.524m-by-0.524m in which a turbulent jet is discharged into the tunnel center via a copper pipe. The pipe has an internal diameter $D = 11$mm, and the exiting flow is that of a fully-developed turbulent pipe flow. Simultaneous measurements of the jet's velocity and density fields were made at $16D$ downstream from the pipe exit using stereoscopic (SPIV) and planar laser-induced fluorescence (PLIF). The combined measurement system was operated at high imaging frame rates together with two high repetition rate lasers - a green laser and a UV laser. The jet material is either pure SF_6 gas or air, giving a VD SF_6-into-air turbulent jet or a air-into-air turbulent jet. The latter is a Boussinesq flow and serves as the control experiment for the VD jet. For binary systems involving the mixing of two fluids, the Atwood number $At = (\rho_{\text{heavy}} - \rho_{\text{light}})/(\rho_{\text{heavy}} + \rho_{\text{light}})$ characterizes the strength of VD effects. At the pipe exit, it is equal to 0.69 and 0 for the SF_6 jet and air jet, respectively. In this talk, we will focus on the velocity field data and look at the small-scale kinematics using the statistics of A_{ij}.
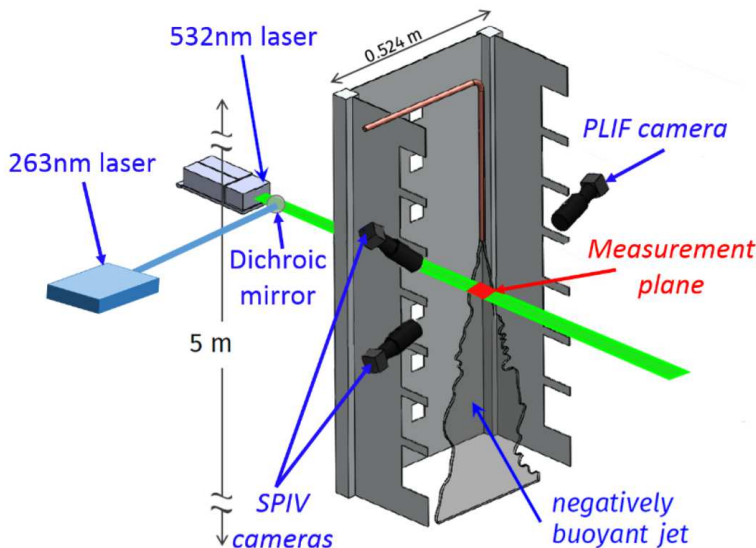

Figure 1: Experimental facility in the present study - an open-circuit wind tunnel having a turbulent jet discharged into a coflowing stream of air. A combined, high-speed, simultaneous stereoscopic PIV and planar LIF system is used to measure both velocity and density fields at a jet cross-section that is $16D$ (jet diameter $D = 11$mm) downstream from the jet nozzle.

Because of the inherent PIV measurement noise, the raw 2D3C data have been filtered by a 2D Gaussian kernel at the two-dimensional measurement plane. The Gaussian kernel has a full width at half maximum (FWHW) equals to two times the size of the PIV interrogation window. Our approach is different from that adopted by Ganapathisubramani et al. (2008) who used a 3D Gaussian kernel; the computed statistics of the fine scales from the present data using a 3D kernel are less satisfactory. Table 1 tabulates the relevant flow parameters of the two jets in the present study. At the measurement station, both jets had a turbulent Reynolds number on the order of $Re_\lambda \sim 100$. The temporal sampling resolution is smaller than one-half of the Kolmogorov time scale, and thus, satisfying the Nyquist-Shannon sampling criterion. The experimental spatial resolution expressed in terms of the Kolmogorov length scale η is between 4-6η in both jets. To resolve the smallest dissipative scales in turbulent flows, a spatial resolution comparable to η is required. However, for VGT statistics, in particular the characteristic "teardrop" shape in the QR-plot, it

Flow property at $x_1 = 16D$	Air jet	SF$_6$ jet
Mean axial velocity, U_1 (m/s)	4.5	6.0
Tunnel coflow velocity, U_a (m/s)	1.3	0.7
Root-mean-square axial velocity, $u_{1,\text{rms}}$ (m/s)	0.69	0.84
Velocity half-width, $b_{1/2}$ (mm)	12	9.1
Taylor microscale, $\lambda = \sqrt{15 \mu u_{1,\text{rms}}^2 / \rho \overline{\varepsilon_{\text{full}}}}$ (mm)	3.24	3
Kolmogorov length scale based on $\overline{\varepsilon_{\text{full}}}$, η (mm)	0.15	0.09
Kolmogorov time scale based on $\overline{\varepsilon_{\text{full}}}$, τ_η (ms)	1.2	0.93
Experimental spatial resolution	$3.7\eta \times 3.7\eta$	$6\eta \times 6\eta$
Experimental temporal resolution	$0.37\tau_\eta$	$0.48\tau_\eta$
Estimated mean dissipation rate, $\overline{\varepsilon_{\text{est}}}$ (m^2/s^3)	9.7	9.7
Mean dissipation rate based on full VGT, $\overline{\varepsilon_{\text{full}}}$ (m^2/s^3)	12.5	10.5
Mean dissipation rate based on local axisymmetric turbulence, $\overline{\varepsilon_{\text{axi}}}$ (m^2/s^3)	12.1	10
Jet Reynolds number $Re = \rho U_o D / \mu$	3150	12856
Turbulent Reynolds number $Re_\lambda = \rho u_{1,\text{rms}} \lambda / \mu$	127	280

Table 1: Flow properties of the present jets. Jet diameter $D = 11$mm, jet exit velocity $U_o = 5.26$m/s, and the dynamic viscosity of air and SF$_6$ gas is $\mu = 1.8 \times 10^{-5}$kg/m/s. The gas density ρ is taken from the data reported in Charonko and Prestridge (2017).

has been shown that this is reliant upon a mix of dissipative and inertial range scales larger than the Taylor microscale λ (Buxton et al., 2017). The spatial resolutions of the present data satisfy this criteria (the ratio $\lambda/\eta = 24 - 33$ in table 1). Another criterion to check the adequacy of spatial resolution is based on the velocity derivative skewness Sk - a third order velocity statistic related to the vortex-stretching term $\omega_i s_{ij} \omega_j$. For a wide range of turbulent flows with Re_λ in the range 10^2-10^3 and in different configurations, Sk is in the range -0.3 to -0.5 (Sreenivasan and Antonia, 1997). Here, we have taken Sk to be equal to the average value of the skewness of the three normal derivatives A_{11}, A_{22} and A_{33}. For the air jet, $Sk = -0.34$ and the value of skewness for each normal derivative is (-0.36,-0.33,-0.33). These near-equal values suggest that vortex-stretching is isotropic in space at the small-scales (Lai et al., 2018).

$$\overline{\varepsilon_{\text{full}}} = \frac{\mu}{\rho}\overline{A_{ij}A_{ij}}, \qquad \overline{\varepsilon_{\text{axi}}} = \frac{\mu}{\rho}\Big[\frac{5}{3}\overline{A_{11}^2} + 2\overline{A_{13}^2} + 2\overline{A_{21}^2} + \frac{8}{3}\overline{A_{23}^2}\Big], \qquad \overline{\varepsilon_{\text{est}}} = 48\frac{U_o^3}{D}\Big(\frac{D}{x_1}\Big)^4 \tag{5}$$

In table 1, we also show the mean turbulent dissipation rate computed with the local axisymmetric turbulence expression $\overline{\varepsilon_{\text{axi}}}$ shown in eq.5 (George and Hussein, 1991). For both jets, this value is within $\pm 5\%$ of that obtained using the full VGT $\overline{\varepsilon_{\text{full}}}$. The standard deviation of the ratio $\overline{\varepsilon_{\text{full}}}/\overline{\varepsilon_{\text{axi}}}$ is about 0.06 for both jets, showing that the conditions of local axisymmetric turbulence are satisfied. The dissipation computed based on the measured velocity gradients is also closed to, but larger than, the estimate $\overline{\varepsilon_{\text{est}}}$ based on large-scale flow properties.

An example of the reconstructed volume of an air jet is shown on the left panel in Figure 2. We have validated our results to those reported in the earlier study by Ganapathisubramani et al. (2008). An example is shown on the right panel of Figure 2; the probability density functions (PDF) of the alignment cosine angles between the vorticity vector and the eigenvectors ($\mathbf{e}_\alpha, \mathbf{e}_\beta, \mathbf{e}_\gamma$) of $\mathbf{s}$ from both studies are in good agreement - ω and $\mathbf{e}_\beta$, the intermediate extensive eigenvector, are preferentially aligned.

4 Results

Figure 3 shows the PDFs of the three normalized eigenvalues $(\alpha, \beta, \gamma) \times \eta^2/\nu$ of $\mathbf{s}$ (left panel). Common to both jets, the mean values behave as $\bar{\alpha}, \bar{\beta} > 0$ and $\bar{\gamma} < 0$ with $|\bar{\gamma}| > \bar{\alpha} > \bar{\beta}$. The weakly positive $\bar{\beta}$ indicates that a fluid element has on average two mutually orthogonal axes in extension (together with $\bar{\alpha}$) which suggests that sheet-like flow structures are statistically more common than tube-like ones, and this tendency is unaltered by VD effects. Fluid elements in the SF$_6$ jet, however, experienced weaker deformations as seen in the smaller magnitudes of the eigenvalues (dashed lines). This agrees with the smaller growth rate (0.052)
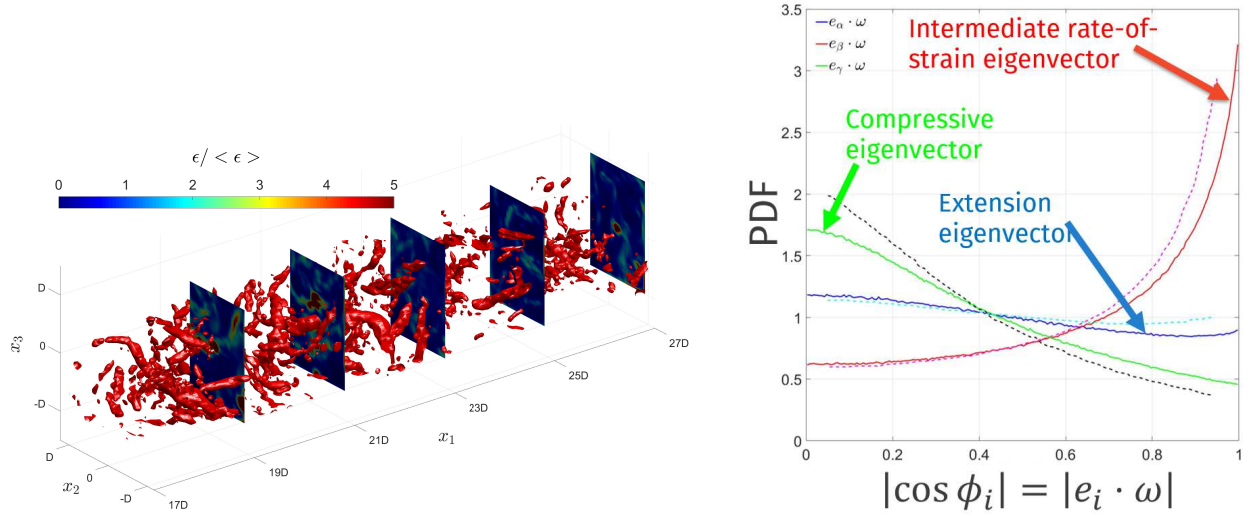
Figure 2: (Left) An example of the reconstructed air jet volume using high-speed SPIV data at a jet cross-section. x_1 is the streamwise direction, and (x_2, x_3) are the two in-plane orthogonal directions of the jet cross-section. Turbulent vortices are visualized in red using the Q-criterion. The cut planes show contours of the viscous dissipation field - highly dissipative regions surround turbulent vortices. (Right) Probability density function of the alignment cosine angles between the eigenvectors of the velocity gradient tensor $\partial u_i / \partial x_j$ and the vorticity vector ω in an air jet - solid lines are from present experiments and dotted lines are from experimental data in Ganapathisubramani et al. (2008).

of the SF_6 jet velocity half-width when compared to that (0.068) of the air jet (Charonko and Prestridge, 2017). On the right panel of figure 3, we plot the PDF of the normalized vortex-stretching term $\omega_i s_{ij} \omega_j$. It is well-known that its mean is positive in turbulent flows, and this fact is observed in the both jets. The comparison on the results of the present air jet (blue solid line) between and that in Ganapathisubramani et al. (2008) (black solid line) is very good. It is interesting to see that the SF_6 jet had a much weaker normalized vortex-stretching than the constant-density jets.

In table 2, we compare the statistics of the fine scales from the present two jets with those from forced homogeneous isotropic turbulence (HIT) (Li et al., 2008, DNS data) and from an atmospheric surface boundary layer (Kohlmyansky et al., 2001, field data). For HIT, it can be shown analytically that $\overline{\omega_i^2} = 2\overline{s_{ij}s_{ij}}$ and $\overline{\omega_i s_{ij} \omega_j} = -\frac{4}{3}\overline{s_{ij}s_{jk}s_{ki}}$. These two relations are not strictly satisfied in both of our jets and in the field data, all of which are heterogeneous, but are accurate to within 10%. The skewness $-\overline{\alpha^3}$ and $-\overline{\gamma^3}$, normalized by the strain self-amplification term, of the most extensive (α) and compressive (γ) eignevalues of $\mathbf{s}$ are quite similar among the heterogeneous flows but are larger than those of HIT in magnitude. The same can be said for the three components, $\overline{\omega_k^2 \lambda_i \cos^2(\omega, e_i)}$, of the vortex-stretching term $\overline{\omega_i s_{ij} \omega_j}$. We, however, note that the magnitudes of $\overline{\omega_k^2 \alpha \cos^2(\omega, e_\alpha)}$ and $|\overline{\omega_k^2 \gamma \cos^2(\omega, e_\gamma)}|$ appear to be enhanced (by about 15-20% compared to the air jet and field data) in the variable-density SF_6 jet. The simultaneous enhancement in these two terms is due to the "near" incompressibility of the flow - it holds strictly for incompressible flows. Finally, it is interesting to see that the contribution by the intermediate eigenvalue β to vortex stretching and strain self-amplification is not affected by density gradients at all.

The vortex-stretching term involves the alignment of the vorticity vector with the eigenframe of the rate-of-strain tensor. Since $\cos(\omega, \mathbf{W}) = \omega \cdot \mathbf{W} / |\omega||\mathbf{W}|$, the magnitude of vortex-stretching is dependent on the alignment cosine angle between ω and the vortex stretching vector $\mathbf{W} = \omega_j s_{ij}$. In figure 4, we see that the PDF of this alignment angle skewed towards positive values - as required by a $\overline{\omega_i s_{ij} \omega_j} > 0$ - for all flows included here. Density gradients in the SF_6 jet do not change this behavior. The PDFs of all heterogeneous flows collapse quite nicely to each other whereas that of HIT is more positively skewed. This last observation can be understood from the ratio of the average of the vortex stretching term and the vortex compression
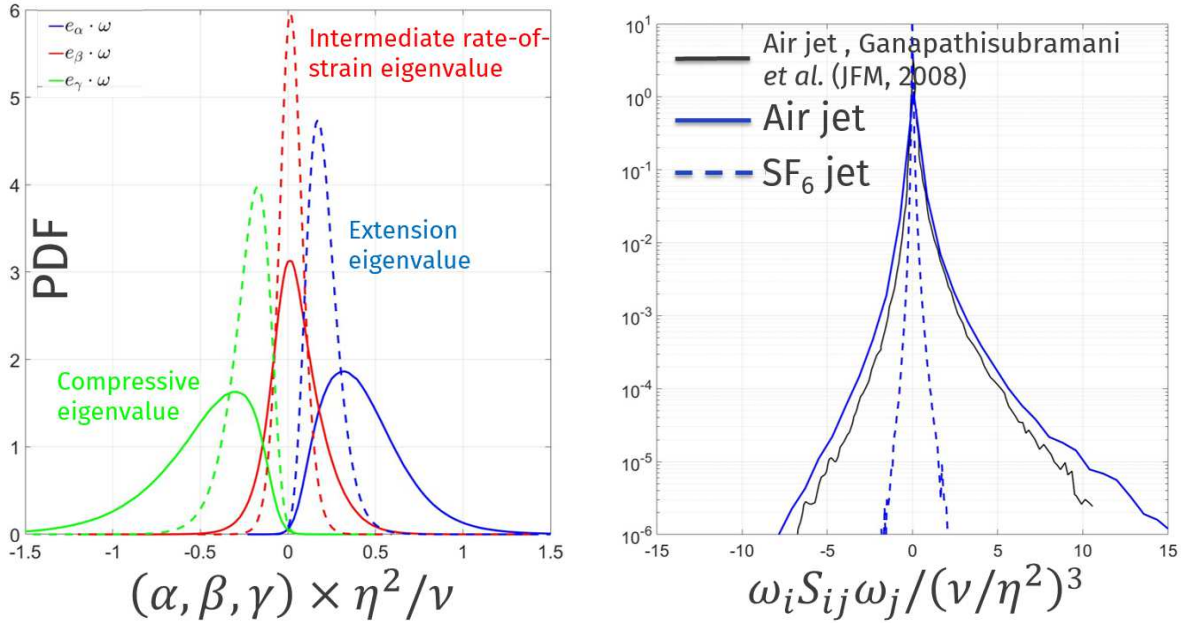
Figure 3: Probability density functions of (left) eigenvalues of the velocity gradient tensor $\partial u_i / \partial x_j$ and (right) the vortex-stretching $\omega_i S_{ij} \omega_j$ term in the enstrophy ω^2-equation. Solid lines are data from a constant-density air jet and dashed lines are data from a variable-density SF_6 jet.

term in table 2 - this ratio is 1.85 for HIT and about 1.6 for the other three heterogeneous flows.

Because vortex-stretching and dissipation are intimately linked to the notion of energy cascade in turbulent flows, we look at the correlation coefficients of $\omega_i s_{ij} \omega_j$ and $s_{ij} s_{jk} s_{ki}$ with enstrophy and strain magnitude in table 3. It should be noted that viscous dissipation is proportional to the square of strain magnitude, $\varepsilon = \nu s_{ij} s_{ij}$, the strain self-amplification term controls the growth and decay of dissipation (eq.(1)).

We now look at the joint PDF of Q and R and study flow topologies in a statistical sense. To ensure the accuracy of present statistical results, we include only data points that have a velocity divergence error $|P = \frac{\partial u_i}{\partial x_i}|$ less than $0.08(\nu/\eta^2)$, as in Gomes-Fernandes et al. (2014), in figures 5-7. This divergence error criterion retains 36% and 25% of the full dataset for the air jet and SF_6, respectively. In both cases, the number of retained data points is between 8-10 millions. In figure 5, we present the QR plots measured in both jets. The probability contours are plotted from 10^{-1} to 10^{-5}. It is evident that the characteristic "teardrop" shape is seen in both jets. However, the area bounded by the 10^{-5} contour is smaller for the variable-density SF_6 jet, a reflection of a smaller normalized vortex-stretching term shown in figure 3.

Figure 6 shows the joint PDFs of the invariants of the rate-of-strain tensor, Q_s and R_s. This plot is used to diagnose the topology of regions in the flow with high strain rates *i.e.* dissipation. It can be seen that both jets have very similar results - the probability contours are biased towards positive values of R_s. Because $R_s = -s_{ij} s_{jk} s_{ki}/3 = -\alpha\beta\gamma$, R_s takes the sign of β, where $R_s > 0$ means that there are two extension principal directions that give rise to sheet-like structures. Further, the maximum of each contour does not lie on the right branch of the Veillefosse tail (Chong et al., 1990, black solid line, $R_s > 0$). Instead, the maxima lie in a region sandwiched between the Veillefosse tail and the red line representing a bi-axial stretching state - this state is characterized by eigenvalues of $\mathbf{s}$ having the ratios $\alpha : \beta : \gamma = 3 : 1 : -4$. This result is in agreement to those reported in many other turbulent flow configurations. Density gradients inside the SF_6 jet do not seem to alter this general observation.

Figure 7 shows the joint PDFs of Q_s and Q_Ω. This plot tells us whether vortex tubes or irrotational dissipative structures are favored in a turbulent flow. The diagonal line (dashed line) represents vortex sheet where

Statistics	Turbulent flows			
	Forced HIT* JHU Database	Air jet Present data	VD SF$_6$ jet Present data	ASL* Kohlmyansky *et al.* (2001)
$\overline{\omega_i^2}/\overline{s_{ij}s_{ij}}$	2	1.87	1.86	< 2
$-\overline{\omega_i s_{ij}\omega_j}/\overline{s_{ij}s_{jk}s_{ki}}$	1.32	1.25	1.27	< 1.33
$-\overline{\alpha^3}/\overline{s_{ij}s_{jk}s_{ki}}$	1.10	1.64	1.93	1.62
$-\overline{\beta^3}/\overline{s_{ij}s_{jk}s_{ki}}$	0.05	0.05	0.05	0.05
$-\overline{\gamma^3}/\overline{s_{ij}s_{jk}s_{ki}}$	-2.16	-2.69	-2.98	-2.67
$\overline{\omega_k^2\,\alpha\cos^2(\omega,e_\alpha)}/\overline{\omega_i s_{ij}\omega_j}$	0.89	1.53	1.71	1.44
$\overline{\omega_k^2\,\beta\cos^2(\omega,e_\beta)}/\overline{\omega_i s_{ij}\omega_j}$	0.59	0.40	0.40	0.47
$\overline{\omega_k^2\,\gamma\cos^2(\omega,e_\gamma)}/\overline{\omega_i s_{ij}\omega_j}$	-0.48	-0.93	-1.11	-0.91
$\overline{\omega_k^2\,\alpha\cos^2(\omega,e_\alpha)}/|\overline{\omega_k^2\,\gamma\cos^2(\omega,e_\gamma)}|$	1.85	1.65	1.54	1.58
Re_λ	433	122	280	10^4

Table 2: Statistical results of the fine scales in various turbulent flows. (α,β,γ) are eigenvalues of the rate-of-strain tensor **s**. *Direct numerical simulation data from (Li et al., 2008). *Atmospheric surface layer (ASL) field data from Kohlmyansky et al. (2001).

	Turbulent flows - (HIT*, air jet, SF$_6$, ASL*)			
	$\omega_i s_{ij}\omega_j$	$-s_{ij}s_{jk}s_{ki}$	$\omega_i s_{ij}\omega_j/\omega_i^2$	$-s_{ij}s_{jk}s_{ki}/s_{ij}^2$
ω_i^2	(0.55,0.37,0.34,0.36)	(0.31,0.17,0.17,0.14)	(0.14,0.12,0.11,0.13)	(0.17,0.10,0.08,0.10)
s_{ij}^2	(0.47,0.34,0.32,0.30)	(0.78,0.68,0.64,0.38)	(0.39,0.30,0.26,0.23)	(0.54,0.46,0.41,0.28)
$-s_{ij}s_{jk}s_{ki}$	(0.54,0.39,0.40,0.15)	/	/	/
$-s_{ij}s_{jk}s_{ki}/s_{ij}^2$	/	/	(0.48,0.29,0.28,0.02)	/

Table 3: Correlation coefficients of the vortex-stretching term $\omega_i s_{ij}\omega_j$ and strain self-amplification term $s_{ij}s_{jk}s_{ki}$ with enstrophy ω_i^2 and strain magnitude $s_{ij}s_{ij}$. *Direct numerical simulation data from (Li et al., 2008). *Atmospheric surface layer (ASL) field data from Kohlmyansky et al. (2001).
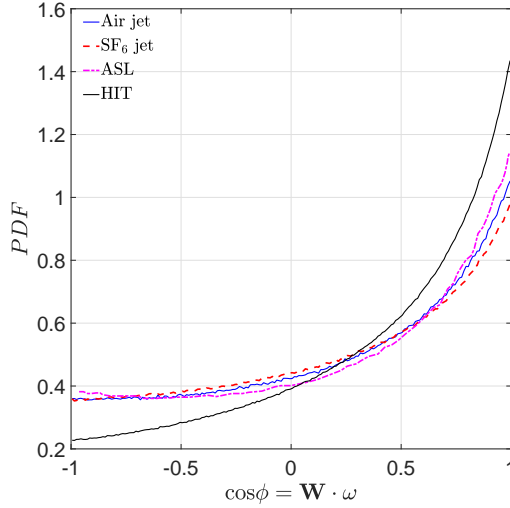
Figure 4: Probability density function of the alignment cosine angle between vorticity ω and vortex stretching vector $\mathbf{W} = \omega_j s_{ij}$. HIT - direct numerical simulation data from (Li et al., 2008). ASL - atmospheric surface layer field data from Kohlmyansky et al. (2001).

QR-quadrants	Proportion of total volume (%)			
	Forced HIT*	Air jet		SF$_6$ jet
	JHU Database	Buxton10*	Present data	Present data
S1	27.3	29	32.6	32.9
S2	26.5	24	19.5	18.7
S3	10	10	11.3	11.3
S4	36.2	37	36.6	37.1

Table 4: Data fraction corresponding to each of the four quadrants $S1$ to $S4$ in a QR-plot. *Direct numerical simulation data from (Li et al., 2008). *Experimental data from Buxton and Ganapathisubramani (2010).

$-Q_s = Q_\Omega$. Again, the results for both jets are similar with vortex tubes being more favorable in regions with high Q_Ω values *i.e.* enstrophy - the maximum value of Q_Ω is always greater than that of $-Q_s$ on such probability contours. Density gradients inside the SF$_6$ jet do not modify this propensity of turbulent flows.

To study the role of different flow structures on the generation/destruction of enstrophy, we consider conditional statistics based on the different quadrants in the QR-plots shown in figure 5 (Buxton and Ganapathisubramani, 2010). Four quadrants $\{S_N\}_{N=1,2,3,4}$ can be defined using the Veillefosse tails and the vertical line $R = 0$. Of events in the four quadrants, only events lying within S1 are capable of enstrophy destruction *i.e.* decreasing enstrophy by compression. The quadrant S4 is mainly responsible for enstrophy amplification via the inviscid mechanism of vortex-stretching. We first look at the data fraction of each quadrant in table 4. Not surprisingly, S4 has the highest data fraction because of the teardrop shape - about 37% of the total flow is swirling and is being stretched along its rotational axis. The second most populated quadrant is S1 where the flow is swirling but is under compression. S2 signifies flow with high strain rates, hence dissipative structures, and accounts for about 20% of the total. From a comparison between previous and the present data, it appears that the distribution of these data fractions/flow structures is not strongly altered by density gradients (table 4).

We now turn to the contributions to the vortex-stretching term $\overline{\omega_i s_{ij} \omega_j}$ from the different flow structures found in the QR-plot in table 5, *i.e.*, the conditional contribution $(\overline{\omega_i s_{ij} \omega_j})_{Si}$. Previous data from constant-density flows, forced homogeneous isotropic turbulence (HIT)($Re_\lambda = 433$) (Li et al., 2008) and an air jet ($Re_\lambda = 160$) (Buxton and Ganapathisubramani, 2010), are added for comparison. S1 is the only quadrant capable of reducing enstrophy, termed enstrophy destruction in Buxton and Ganapathisubramani (2010), among the four quadrants. S4 is the quadrant dominating the production of enstrophy, and S2 and S3 are
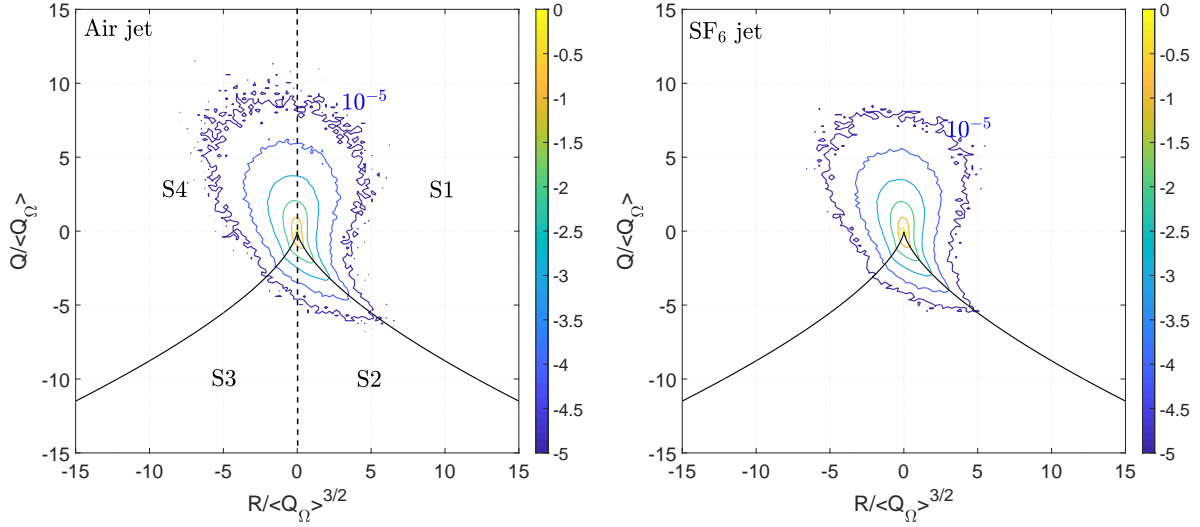
Figure 5: Joint probability density functions of the second Q and third R invariants of the velocity gradient tensor $\partial u_i / \partial x_j$ in an air jet (left) and a SF_6 jet (right). The contours are probability densities plotted on a $\log_{10}$ scale. $Q_\Omega = \frac{1}{4} \omega_i^2$ is the second invariant of the spin tensor Ω. The QR-plot can be divided into four regions, $\{S_N\}_{N=1,2,3,4}$, to analyze the contributions of different flow structures to the production of enstrophy. The shown data are conditioned to have values of $|P| < 0.08 (\nu / \eta^2)$.

QR-quadrants		$(\overline{\omega_i s_{ij} \omega_j})_{S_N} / \overline{\omega_i s_{ij} \omega_j}$		
	Forced HIT*		Air jet	SF_6 jet
	JHU Database	Buxton10*	Present data	Present data
S1	-0.48	-0.40	-0.36	-1.0
S2	0.75	0.69	0.72	0.64
S3	0.48	0.54	0.73	0.77
S4	2.44	2.44	2.66	3.10

Table 5: Different contributions $(\overline{\omega_i s_{ij} \omega_j})_{S_N}$ to the total vortex-stretching term $\overline{\omega_i s_{ij} \omega_j}$ conditioned on the four quadrants $S1$ to $S4$ in a QR-plot. *Direct numerical simulation data from (Li et al., 2008). *Experimental data from Buxton and Ganapathisubramani (2010).

comparable in their positive contributions to enstrophy.

5 Conclusion

This study investigates the small-scale kinematics of a turbulent, variable-density SF_6 jet. To obtain the required three-dimensional velocity fields, we have reconstructed pseudo volumes of the jet by applying Taylor's *frozen turbulence* hypothesis to a time-resolved stereoscopic PIV dataset obtained at a jet cross-section. We have found the following results for the variable-density jet: (1) it experiences weaker (in magnitude) fluid deformation, (2) it has a weaker normalized vortex-stretching term, (3) its QR-plot exhibits a teardrop shape, (4) the density gradients do not seem to alter the propensity to form tube-like swirling structures surrounded by sheet-like, highly dissipative structures, and (5) conditional statistics based on the different quadrants in the QR-plot show that it has stronger enstrophy production/destruction contributions to the total $\omega_i S_{ij} \omega_j$ than that observed in the air jet.

Based on this work, laboratory experiments are currently underway to combine time-resolved stereoscopic PIV and planar laser-induced fluorescence (PLIF) to obtain simultaneous volumetric velocity and density fields. These results will be used to better understand the interplay of density gradients with velocity in the VD jet.
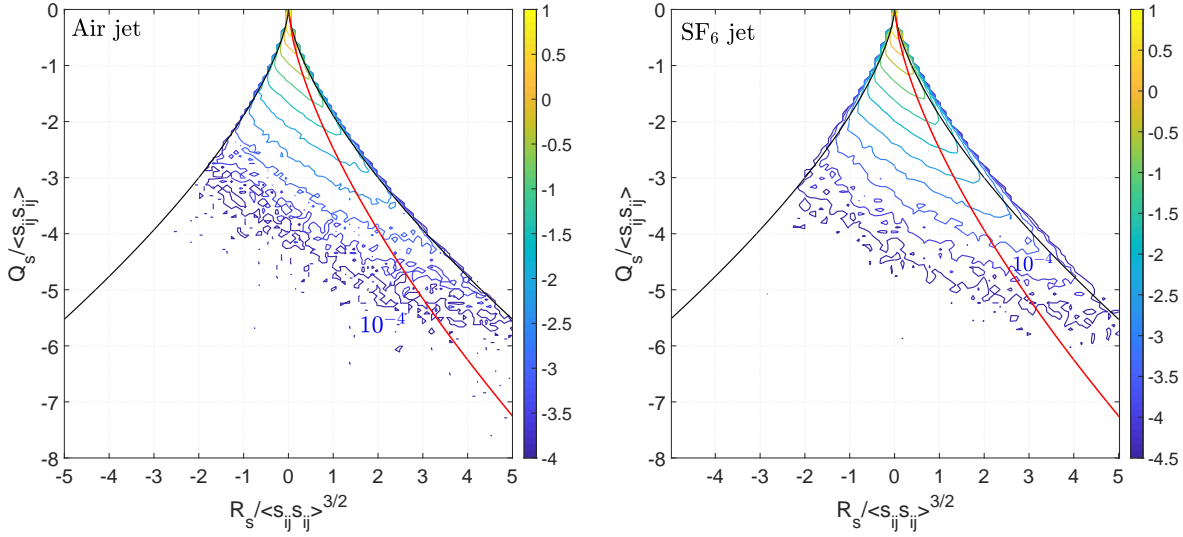
Figure 6: Joint probability density functions of the second Q_s and third R_s invariants of the rate-of-strain tensor s_{ij} in an air jet (left) and a SF_6 jet (right). The contours are probability densities plotted on a $\log_{10}$ scale. The red solid line represents $R_s = (-Q_s)^{3/2} a(1+a)(1+a+a^2)^{-3/2}$ where $a = \beta/\alpha = 1/3$, and the ratio of eigenvalues of $\mathbf{s}$ are $\alpha : \beta : \gamma = 3 : 1 : -4$. The shown data are conditioned to have values of $|P| < 0.08(\nu/\eta^2)$.

References

Buxton O, Breda M, and Chen X (2017) Invariants of the velocity gradient tensor in a spatially developing inhomogeneous turbulent flow. *Journal of Fluid Mechanics* 817:1–20

Buxton O and Ganapathisubramani B (2010) Amplification of enstrophy in the far field of an axisymmetric turbulent jet. *Journal of Fluid Mechanics* 651:483–502

Charonko J and Prestridge K (2017) Variable-density mixing in turbulent jets with coflow. *Journal of Fluid Mechanics* 825:887–921

Chong M, Perry A, and Cantwell B (1990) A general classification of three-dimensional flow fields. *Phys Fluids* 2(5):765–777

Ganapathisubramani B, Lakshminarasimhan K, and Clemens N (2008) A general classification of three-dimensional flow fields. *Phys Fluids* 2:765–777

George W and Hussein H (1991) Locally axisymmetric turbulence. *Journal of Fluid Mechanics* 233:1–23

Gomes-Fernandes R, Ganapathisubramani B, and Vassilicos J (2014) Evolution of the velocity-gradient tensor in a spatially developing turbulent flow. *Journal of Fluid Mechanics* 756:252–292

Kohlmyansky M, Tsinober A, and Yorish S (2001) Velocity derivatives in the atmospheric surface layer at $re_\lambda = 10^4$. *Phys Fluids* 13:311–314

Lai C, Charonko J, and Prestridge K (2018) A karman-howarth-monin equation for variable-density turbulence. *Journal of Fluid Mechanics* 843:382–418

Li Y, Perlman E, Wan M, Yang Y, Meneveau C, Burns R, Chen S, Szalay A, and Eyink G (2008) A public turbulence database cluster and applications to study lagrangian evolution of velocity increments in turbulence. *J Turbul* 9:N31

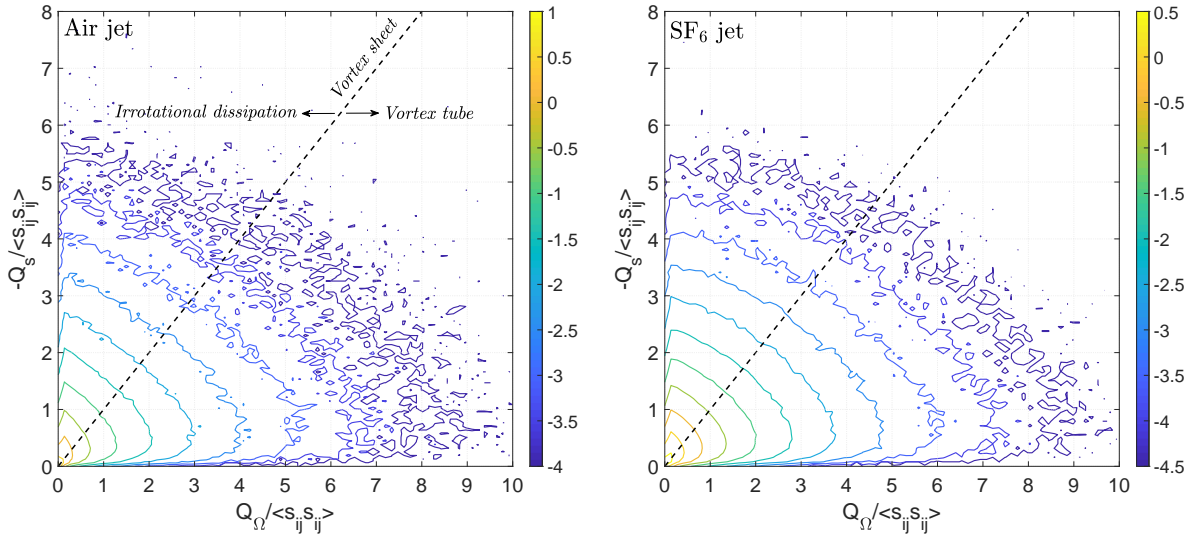Livescu D and Ristorcelli J (2007) Buoyancy-driven variable-density turbulence. *Journal of Fluid Mechanics* 591:43–71

Figure 7: Joint probability density functions of the second invariants (Q_s, Q_Ω) of the rate-of-strain s_{ij} and spin Ω_{ij} tensors in an air jet (left) and a SF_6 jet (right). The contours are probability densities plotted on a $\log_{10}$ scale. The shown data are conditioned to have values of $|P| < 0.08(\nu/\eta^2)$.

Livescu D and Ristorcelli J (2008) Variable-density mixing in buoyancy-driven turbulence. *Journal of Fluid Mechanics* 605:145–180

Meneveau C (2011) Lagrangian dynamics and models of the velocity gradient tensor in turbulent flows. *Annual Review of Fluid Mechanics* 43:219–245

Ooi A, Martin J, Soria J, and Chong M (1999) A study of the evolution and characteristics of the invariants of the velocity-gradient tensor in isotropic turbulence. *Journal of Fluid Mechanics* 381:141–174

Pope S (2000) *Turbulent Flows*. Cambridge University Press. 1st edition

Sreenivasan K and Antonia R (1997) The phenomenology of small-scale turbulence. *Annu Rev Fluid Mech* 29:435

Tsinober A (2009) *An informal conceptual introduction to turbulence*. Fluid mechanics and its application (Book 92). Springer. 2nd edition

Westerweel J, Elsinga G, and Adrian R (2013) Particle image velocimetry for complex and turbulent flows. *Annu Rev Fluid Mech* 45:409–436

Zhang J, Tao B, and Katz J (1997) Turbulent flow measurement in a square duct with hybrid holographic piv. *Exp Fluids* 23:373–381